2 Absorption and scattering by molecules and particles

Jacqueline Lenoble, Michael I. Mishchenko, and Maurice Herman

2.1 Introduction

The Earth's atmosphere absorbs, scatters, and emits electromagnetic radiation. Although air molecules are the primary actors in these processes, aerosol particles are also present ubiquitously (see Chapter 1) and modify the radiation field. In fact, this modification constitutes the very physical basis of aerosol remote sensing. Whenever clouds are present, they have a much larger influence on radiation which largely overshadows the aerosol impact. Therefore, in aerosol remote sensing, one often has to limit observations to cloudless conditions and screen cloudy pixels.

In the solar part of the spectrum, molecular absorption is mostly limited to ultraviolet (UV; ozone) and near-infrared (near-IR; carbon dioxide, water vapor) wavelengths and is characterized by strong and narrow oxygen bands. A brief description of atmospheric molecular absorption is presented in Section 2.2. Shortwave aerosol remote sensing is usually performed outside the absorption bands, but some instruments also have channels capturing absorption bands with the objective of quantifying gaseous components.

Absorption in the longwave terrestrial spectrum, both by molecules and aerosols, is accompanied by emission, according to Kirchhoff's law. This subject will be addressed in Chapter 9.

In Sections 2.3 and 2.4, we present some basic definitions concerning the scattering and polarization phenomena; the same formalism will be used throughout this book. Section 2.5 deals with Rayleigh molecular scattering, Section 2.6 summarizes the theory of scattering by spherical particles (the Lorenz–Mie theory), and Section 2.7 addresses the scattering by nonspherical particles. Finally, in Section 2.8, we discuss the main traits of single-scattering and absorption characteristics of spherical and nonspherical aerosols.

J. Lenoble et al. (eds.), *Aerosol Remote Sensing*, Springer Praxis Books,
DOI 10.1007/978-3-642-17725-5_2, © Springer-Verlag Berlin Heidelberg 2013

2.2 Atmospheric molecular absorption

Solar radiation at very short wavelengths is strongly absorbed in the upper atmosphere, mainly by oxygen in the Schumann–Runge and Herzberg bands (Greenblatt et al., 1990), and, therefore, is not very useful for remote sensing. At wavelengths above 250 nm, the ozone absorption becomes dominant, in the Hartley and Huggins bands, and limits the ability to observe the solar spectrum at the Earth's surface around 300 nm. Figure 2.1 depicts the absorption cross-section of ozone in the UV region. The Hartley and Huggins bands do not yield a line structure, but rather cause small oscillations superposed on the continuum. Numerous measurements of the ozone absorption have been performed over the past decades (Vigroux, 1953; Molina and Molina, 1986; Paur and Bass, 1985; Burrows et al., 1999b), especially in the Huggins bands, and have demonstrated the absorption to be strongly temperature dependent. Remote sensing in the UV can be used to retrieve simultaneously aerosols and ozone, as, e.g., with TOMS and OMI instruments (see Chapters 7 and 8). In the visible, ozone causes the much weaker Chappuis absorption band which is not temperature dependent (Amuroso et al., 1990), as shown in Figure 2.2. This band is used in remote sensing with SAGE and similar occultation instruments (see Chapter 8).

Minor gaseous constituents, such as NO_2, NO_3, OClO, and SO_2, also cause some absorption bands in the UV and visible parts of the spectrum, thereby facilitating remote

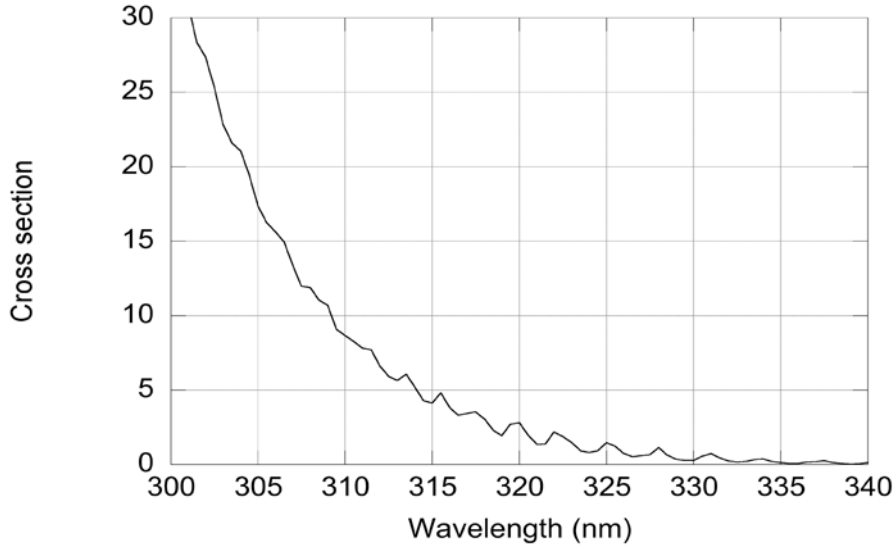

Figure 2.1 Ozone UV absorption cross section $\times 10^{-20}$ (cm^2) at 230 K.

sensing of these gases. The oxygen molecule causes a few narrow bands in the visible and near-IR, the most important bands being centered at 690 and 760 nm. Measurements of the 760-nm band, called the A band, are used in remote sensing of cloud top heights (Fischer and Grassl, 1991).

In the near-IR, besides the strong-absorption bands due to H_2O and CO_2 (see the spectroscopic data banks HITRAN at www.cfa.harvard.edu/hitran, and GEISA at ether.ipsl.jussieu.fr), several species cause absorption bands also used for remote sensing. However, this topic is beyond the scope of our discussion of aerosol remote sensing.

2.3 Definitions: Extinction, scattering, absorption, and phase function

The radiative energy is most generally characterized by the radiant flux density (Wm^{-2}); for simplicity it is called intensity I in this chapter, without considering its distribution in directions; I takes generally the name of irradiance, when received on a surface. In Chapter 3, we will define the radiance L ($Wm^{-2}sr^{-1}$), used in radiative transfer analysis.

Let us consider a horizontal layer of infinitesimal thickness ds inside the atmosphere or any other medium composed of sparsely distributed scatterers (Figure 2.3a). A paral-

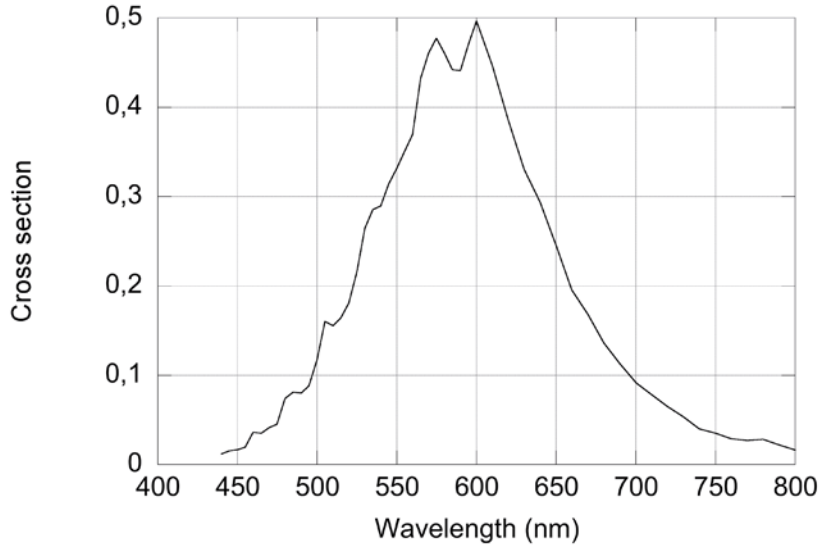

Figure 2.2 Ozone visible absorption cross section $\times 10^{-20}$ (cm^2).

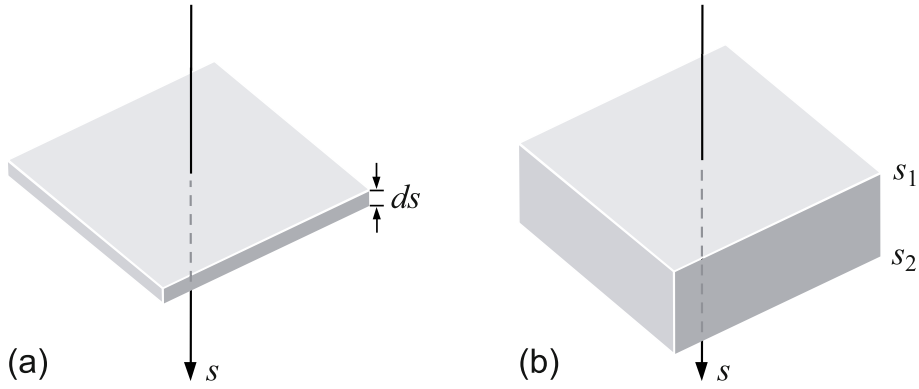

Figure 2.3 Definition of extinction.

lel beam of monochromatic radiation incident from above perpendicularly to this layer is characterized by its intensity I (Wm^{-2}) at the entrance surface of the layer and an intensity $I + dI$ at the exit surface. According to the microphysical theory of radiative transfer (Mishchenko et al., 2006), dI is proportional to the product of I and ds:

$$dI = -\sigma_e I ds, \tag{2.1}$$

where σ_e (m^{-1}) is the local extinction coefficient. Implicit in Eq. (2.1) is the assumption that the scattering medium is composed of spherically symmetric and/or randomly oriented nonspherical particles. Preferential orientation of nonspherical particles requires the introduction of a 4 × 4 extinction-matrix coefficient rather than the scalar extinction coefficient (Mishchenko et al., 2006).

The cumulative extinction is generally due to two different physical phenomena: absorption, wherein the radiative energy is transformed into another form of energy (e.g., via heating and photochemical reactions), and scattering, wherein a part of the incident light changes its direction of propagation and is lost to the incident energy flux. Both molecules and aerosols absorb and scatter radiation. The extinction coefficient is the sum of the absorption coefficient σ_a and the scattering coefficient σ_s:

$$\sigma_e = \sigma_a + \sigma_s. \tag{2.2}$$

To characterize a molecule or a particle, one generally uses the extinction, absorption, and scattering cross-sections (C_e, C_a, and C_s) expressed in m^2. The extinction, absorption, and

scattering coefficients defined above are obtained by multiplying the respective cross-sections by the number of molecules or particles per unit volume. The fractional contribution of scattering to the total extinction is given by the single-scattering albedo (SSA):

$$\varpi = \sigma_s / \sigma_e. \tag{2.3}$$

For a finite-thickness layer located between s_1 and s_2 (Figure 2.3b), the integration of Eq. (2.1) yields

$$I(s_2) = I(s_1)\exp(-\tau_e), \tag{2.4}$$

where

$$\tau_e = \int_{s_1}^{s_2} \sigma_e(s)ds \tag{2.5}$$

is the optical thickness of the layer and $\exp(-\tau_e)$ is its optical transmittivity. Of course τ_e can be decomposed into the sum of the absorption, τ_a, and scattering, τ_s, optical thicknesses. Quite often the subscript "e" is omitted when implicit from the context. Equation (2.4) is known as Bouguer-Beer's exponential extinction law and, strictly speaking, applies only to monochromatic radiation. However, it can also be applied to narrow wavelength intervals over which the intensity and the extinction vary slowly. This is the case for scattering (both molecular and aerosol), aerosol absorption, and ozone absorption, but not for gaseous line absorption.

In the atmosphere, the optical depth is traditionally measured along a vertical path and is equal to the optical thickness of the atmospheric layer above a given altitude. The total optical thickness of the atmosphere corresponds to the optical depth at the surface level.

The scattered radiation is lost to the initial parallel energy flux and has a probability to be distributed in any direction depending on the specific type of scatterers. In the case of unpolarized incident light (e.g., sunlight), the phase function $p(\Theta)$ expresses this probability as a function of the scattering angle $\Theta \in [0, \pi]$, i.e., the angle between the incidence and scattering directions (see Figure 2.4 showing the plane of scattering defined by these two directions). The amount of monochromatic radiative power scattered by an elementary volume dV of the scattering medium into a solid angle $d\Omega$ around the direction Θ is given by

$$d\tilde{I} = \sigma_s p(\Theta) I dV d\Omega / 4\pi, \tag{2.6}$$

where $\tilde{I}$ is measured in W. The conservation of energy implies that $p(\Theta)$ is normalized to 4π when integrated over all scattering directions. As before, we assume that the scattering medium is composed of spherically symmetric and/or randomly oriented nonspherical particles.

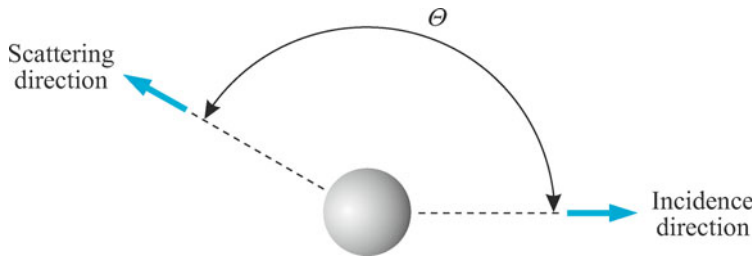

Figure 2.4 Electromagnetic scattering.

It is customary and convenient to expand the phase function in a series of Legendre polynomials P_l:

$$p(\Theta) = \sum_{l=0}^{l=L} \beta_l P_l(\cos\Theta), \tag{2.7}$$

where

$$\beta_l = \frac{2l+1}{2} \int_{-1}^{+1} p(\Theta) P_l(\cos\Theta) d(\cos\Theta); \tag{2.8}$$

the upper summation limit L is 2 for molecules and increases rapidly as the particle size exceeds the incident wavelength (Section 2.8). The normalization of the phase function implies that $\beta_0 = 1$.

The asymmetry factor is defined as

$$g = \langle \cos\Theta \rangle = \int_{-1}^{+1} p(\Theta) \cos\Theta d(\cos\Theta) / \int_{-1}^{+1} p(\Theta) d(\cos\Theta) = \beta_1 / 3. \tag{2.9}$$

A useful analytical representation of the phase function is the Henyey–Greenstein function (Henyey and Greenstein, 1941)

$$p(\Theta) = \frac{1 - g^2}{(1 + g^2 - 2g\cos\Theta)^{3/2}}; \tag{2.10}$$

it is used quite often and usually gives good results in radiative flux computations.

As stated above, the number of terms in the expansion (2.7) increases rapidly for large particles, when the phase function exhibits a very strong forward peak (see Section 2.8). Therefore, a useful approximation is to write the phase function as the sum of a delta-function term and a much smoother phase-function component:

$$p(\Theta) = 2f\Delta(1 - \cos\Theta) + (1 - f)p'(\Theta), \tag{2.11}$$

where $p'(\Theta)$ can be expanded into series of Legendre polynomials with many fewer terms than $p(\Theta)$. Physically, this approximation implies that the radiation scattered in the forward peak is simply transmitted; the constant f is empirically defined, depending on how the forward peak is truncated (Potter, 1970).

2.4 Polarization and scattering matrix

In general, the scattering process modifies the state of polarization of the radiation incident on a molecule or a particle. In order to account for this phenomenon appropriately, especially when one has to deal with two or more successive scattering events (see Chapter 3), it is first necessary to choose a consistent representation of polarized radiation.

2.4.1 The Stokes parameters

A time-harmonic plane electromagnetic wave propagating in the direction of the wave vector $\mathbf{k}$ is characterized by two orthogonal components $\mathbf{E}_l$ and $\mathbf{E}_r$ of its complex electric vector $\mathbf{E}(\mathbf{r}, t) = \mathbf{E}\exp(i\omega t - i\mathbf{k}\cdot\mathbf{r})$ defined in the wave plane (i.e., the plane normal to $\mathbf{k}$), where t is time, $\mathbf{r}$ is the position vector of the observation point, ω is the angular frequency, and $i = \sqrt{-1}$. The subscripts "l" and "r" denote the components parallel and perpendicular to a reference plane, respectively (Figure 2.5).

Because of high frequency of the time-harmonic oscillations, traditional optical instruments cannot measure the electric and magnetic fields associated with the electromagnetic wave. Instead, optical instruments usually measure quantities that have the dimension of energy flux and are combinations of the four products $E_l E_l^*, E_r E_r^*, E_r E_l^*$, and $E_l E_r^*$, where the asterisk denotes a complex-conjugate value. In particular, the real-valued Stokes parameters I, Q, U, and V of the plane wave (Stokes, 1852; Chandrasekhar, 1950) form a so-called Stokes column vector $\mathbf{I}$ defined as

$$\mathbf{I} = \begin{pmatrix} I \\ Q \\ U \\ V \end{pmatrix} = \frac{\varepsilon_0 c}{2} \begin{pmatrix} E_l E_l^* + E_r E_r^* \\ E_l E_l^* - E_r E_r^* \\ E_l E_r^* + E_r E_l^* \\ iE_l E_r^* - iE_r E_l^* \end{pmatrix} = \frac{\varepsilon_0 c}{2} \begin{pmatrix} E_{l0}^2 + E_{r0}^2 \\ E_{l0}^2 - E_{r0}^2 \\ 2E_{l0}E_{r0}\cos\delta \\ 2E_{l0}E_{r0}\sin\delta \end{pmatrix}, \tag{2.12}$$

where E_{l0} and E_{r0} are the amplitudes of the complex time-harmonic components E_l and E_r,

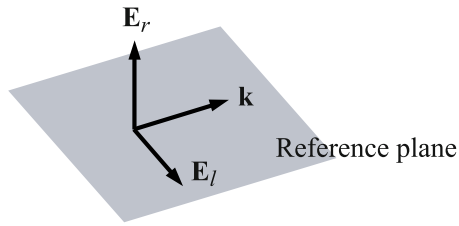

Figure 2.5 Electric field vector components. The reference plane contains the vectors **k** and $\mathbf{E}_l$. The wave plane goes through the vectors $\mathbf{E}_r$ and $\mathbf{E}_l$.

respectively; δ is the retardation in the phase of E_l relative to that of E_r; c is the speed of light in a vacuum; and ε_0 the dielectric constant of a vacuum. All four Stokes parameters have the dimension of the scalar quantity I (Wm^{-2}). If the Stokes vector is associated with radiance, the Stokes parameters are in $\mathrm{Wm}^{-2}\mathrm{sr}^{-1}$.

A plane electromagnetic wave is the simplest type of electromagnetic radiation and is well represented by a perfectly monochromatic and perfectly parallel laser beam. Let us consider an arbitrary point within such a beam. It is straightforward to demonstrate (see, e.g., Mishchenko et al., 2002, 2006) that during each time interval $2\pi/\omega$, the end-point of the real electric field vector $\mathrm{Re}[\mathbf{E}(\mathbf{r},t)]$ describes an ellipse in the wave plane. The sum of the squares of the semi-axes of this ellipse, multiplied by $\varepsilon_0 c/2$, yields the total intensity of the wave I. The ratio of the semi-axes, the orientation of the ellipse, and the sense in which the electric vector rotates (clockwise or counter-clockwise, when looking in the direction of propagation) can be derived from the other three Stokes parameters of the wave, Q, U, and V. Importantly, any plane electromagnetic wave is fully polarized, i.e., satisfies the Stokes identity

$$I^2 \equiv Q^2 + U^2 + V^2. \tag{2.13}$$

Quasi-monochromatic beams of light are encountered much more often than perfectly monochromatic beams and, in general, are described by $\mathbf{E}(\mathbf{r},t) = \mathbf{E}(t)\exp(i\omega t - i\mathbf{k}\cdot r)$, where fluctuations in time of the complex amplitude of the electric field $\mathbf{E}(t)$ around its mean value occur much more slowly than the harmonic oscillations of the time factor $\exp(i\omega t)$, albeit still too fast to be detected by an actual optical detector of electromagnetic energy flux. Therefore, the Stokes parameters measured by the detector are obtained by taking an average of the right-hand side of Eq. (2.12) over a time interval much longer than $2\pi/\omega$:

$$\mathbf{I} = \begin{pmatrix} I \\ Q \\ U \\ V \end{pmatrix} = \frac{\varepsilon_0 c}{2} \begin{pmatrix} \langle E_l E_l^* \rangle + \langle E_r E_r^* \rangle \\ \langle E_l E_l^* \rangle - \langle E_r E_r^* \rangle \\ \langle E_l E_r^* \rangle + \langle E_r E_l^* \rangle \\ i\langle E_l E_r^* \rangle - i\langle E_r E_l^* \rangle \end{pmatrix} = \frac{\varepsilon_0 c}{2} \begin{pmatrix} \langle E_{l0}^2 \rangle + \langle E_{r0}^2 \rangle \\ \langle E_{l0}^2 \rangle - \langle E_{r0}^2 \rangle \\ \langle 2E_{l0}E_{r0}\cos\delta \rangle \\ \langle 2E_{l0}E_{r0}\sin\delta \rangle \end{pmatrix}. \tag{2.14}$$

These average Stokes parameters contain all practically available information on the quasi-monochromatic parallel beam (Chandrasekhar, 1950; Mishchenko et al., 2006). I is the total intensity of the beam considered in the previous section. The other three Stokes parameters have the same dimension as I (Wm^{-2}) and satisfy the inequality

$$I^2 \geq Q^2 + U^2 + V^2. \tag{2.15}$$

In general, the end-point of the vector $\mathrm{Re}[\mathbf{E}(\mathbf{r}, t)]$ of a quasi-monochromatic beam does not describe a well-defined polarization ellipse. Still, one can think of a "preferential" ellipse with a "preferential orientation", "preferential elongation", and "preferential handedness". Equation (2.15) implies that a quasi-monochromatic beam can be partially polarized and even unpolarized. The latter means that the temporal behavior of $\mathrm{Re}[\mathbf{E}(\mathbf{r}, t)]$ is completely "erratic", so that there is no "preferential ellipse". This is, for example, the case for the extraterrestrial solar radiation.

When two or more quasi-monochromatic beams propagating in the same direction are mixed incoherently, which means that there is no permanent phase relation between the separate beams, then the Stokes column vector of the mixture is equal to the sum of the Stokes column vectors of the individual beams:

$$\mathbf{I} = \sum_n \mathbf{I}_n, \tag{2.16}$$

where n numbers the beams. According to Eqs (2.15) and (2.16), it is always possible mathematically to decompose any quasi-monochromatic beam into two incoherent parts, one unpolarized, with a Stokes column vector

$$\begin{bmatrix} I - \sqrt{Q^2 + U^2 + V^2} \\ 0 \\ 0 \\ 0 \end{bmatrix},$$

and one fully polarized, with a Stokes column vector

$$\begin{bmatrix} \sqrt{Q^2 + U^2 + V^2} \\ Q \\ U \\ V \end{bmatrix}.$$

Thus, the intensity of the fully polarized component is $(Q^2 + U^2 + V^2)^{1/2}$, and so the degree of (elliptical) polarization of the quasi-monochromatic beam can, in general, be defined as

$$P = \frac{\sqrt{Q^2 + U^2 + V^2}}{I}. \tag{2.17}$$

The parameters of the "preferential ellipse" of a parallel quasi-monochromatic beam of light can be viewed as quantitative descriptors of the asymmetry in the directional distribution and/or rotation direction distribution of the vector $\mathrm{Re}[\mathbf{E}(\mathbf{r},t)]$ in the wave plane. For example, a common type of polarization encountered in natural conditions is partial or full linear polarization, which implies that the Stokes parameter V is negligibly small. This type of polarization is often described by the total intensity, degree of linear polarization, and angle α defined in the wave plane and specifying the orientation of the plane of preferential oscillations of the real electric field vector with respect to the reference plane (Figure 2.5). The degree of linear polarization is given by

$$P = \frac{\sqrt{Q^2 + U^2}}{I}, \tag{2.18}$$

the second and third Stokes parameters are given by

$$\begin{aligned} Q &= IP\cos 2\alpha, \\ U &= IP\sin 2\alpha, \end{aligned} \tag{2.19}$$

and the orientation angle is given by

$$\alpha = \frac{1}{2}\,\mathrm{arctg}\,(U/V). \tag{2.20}$$

In general, the parameter V is nonzero and defines the preferential ellipticity of the beam. However, V is usually very small in the atmosphere and is often neglected, the polarization being considered (partially) linear.

It is clear from the above discussion that the Stokes parameters are always defined with respect to a reference plane containing the direction of light propagation (Figure 2.5). If the

reference plane is rotated about the direction of propagation then the Stokes parameters are modified according to a rotation transformation rule. Specifically, consider a rotation of the reference plane through an angle $0 \le \chi < 2\pi$ in the anti-clockwise direction when looking in the direction of propagation. Then the new Stokes column vector is given by

$$\mathbf{I}' = \mathbf{T}(\chi)\mathbf{I}, \tag{2.21}$$

where

$$\mathbf{T}(\chi) = \begin{bmatrix} 1 & 0 & 0 & 0 \\ 0 & \cos 2\chi & \sin 2\chi & 0 \\ 0 & -\sin 2\chi & \cos 2\chi & 0 \\ 0 & 0 & 0 & 1 \end{bmatrix} \tag{2.22}$$

is the Stokes rotation matrix for angle χ.

2.4.2 Scattering matrix

Upon choosing the reference axes parallel and perpendicular to the scattering plane for both the incident and scattered radiation, Eq. (2.6) is replaced by

$$d\widetilde{\mathbf{I}} = \sigma_s \mathbf{F}(\Theta)\mathbf{I} dV d\Omega / 4\pi, \tag{2.23}$$

where

$$\mathbf{F}(\Theta) = [F_{ij}(\Theta)], \quad i, j = 1,...,4 \tag{2.24}$$

is the 4×4 so-called normalized Stokes scattering matrix such that $F_{11}(\Theta) = p(\Theta)$. For an ensemble of randomly oriented particles each of which has a plane of symmetry and/or for an ensemble containing an equal number of particles and their mirror counterparts in random orientation, the scattering matrix has the following simplified structure and only six independent elements:

$$\mathbf{F}(\Theta) = \begin{bmatrix} F_{11}(\Theta) & F_{12}(\Theta) & 0 & 0 \\ F_{12}(\Theta) & F_{22}(\Theta) & 0 & 0 \\ 0 & 0 & F_{33}(\Theta) & F_{34}(\Theta) \\ 0 & 0 & -F_{34}(\Theta) & F_{44}(\Theta) \end{bmatrix} \tag{2.25}$$

with

$$F_{12}(0) = F_{12}(\pi) = F_{34}(0) = F_{34}(\pi) = 0, \tag{2.26}$$

$$F_{33}(\pi) = -F_{22}(\pi), \tag{2.27}$$

$$F_{11}(\pi) - 2F_{22}(\pi) - F_{44}(\pi) = 0 \tag{2.28}$$

(van de Hulst, 1957; Mishchenko et al., 2002). Still further simplifications occur for spherical particles:

$$\mathbf{F}(\Theta) = \begin{bmatrix} F_{11}(\Theta) & F_{12}(\Theta) & 0 & 0 \\ F_{12}(\Theta) & F_{11}(\Theta) & 0 & 0 \\ 0 & 0 & F_{33}(\Theta) & F_{34}(\Theta) \\ 0 & 0 & -F_{34}(\Theta) & F_{33}(\Theta) \end{bmatrix}, \tag{2.29}$$

$$F_{33}(0) = F_{11}(0). \tag{2.30}$$

Several recipes can be used to check the physical correctness of the elements of a scattering matrix found as the outcome of laboratory measurements or theoretical computations (Hovenier and van der Mee, 2000).

A useful expansion of the elements of the scattering matrix in so-called generalized spherical functions (Kuščer and Ribarič, 1959; Siewert, 1982; Lenoble et al., 2007) is as follows:

$$\begin{aligned}
F_{11}(\Theta) &= p(\Theta) = \sum_{l=0}^{L} \beta_l P_l(\cos\Theta), \\
F_{21}(\Theta) &= F_{12}(\Theta) = \sum_{l=2}^{L} \gamma_l P_2^l(\cos\Theta), \\
F_{22}(\Theta) &= \sum_{l=2}^{L} [\alpha_l R_2^l(\cos\Theta) + \zeta_l T_2^l(\cos\Theta)], \\
F_{33}(\Theta) &= \sum_{l=2}^{L} [\zeta_l R_2^l(\cos\Theta) + \alpha_l T_2^l(\cos\Theta)], \\
F_{43}(\Theta) &= -F_{34}(\Theta) = \sum_{l=2}^{L} \varepsilon_l P_2^l(\cos\Theta), \\
F_{44}(\Theta) &= \sum_{l=0}^{L} \delta_l P_l(\cos\Theta),
\end{aligned} \tag{2.31}$$

where

$$R_s^l(\cos\Theta) = \frac{1}{2}[P_{s2}^l(\cos\Theta) + P_{s,-2}^l(\cos\Theta)], \tag{2.32a}$$

$$T_s^l(\cos\Theta) = \frac{1}{2}[P_{s2}^l(\cos\Theta) - P_{s,-2}^l(\cos\Theta)]. \tag{2.32b}$$

The $P_{mn}^l(x)$ are the generalized spherical functions introduced by Gel'fand and Shapiro (1956); they reduce to the usual Legendre polynomials P_l for $m = n = 0$. The P_m^l are the standard associated Legendre functions. The first expansion of Eq. (2.31) is, of course, identical to Eq. (2.7). An alternative form of Eq. (2.31) can be found in Mishchenko et al. (2002, 2006), and Hovenier et al. (2004).

2.5 Molecular scattering: Rayleigh theory

The theory of molecular scattering was first developed by Strutt (1871), later known as Lord Rayleigh (1889). He assumed that the incident electromagnetic wave induces an electric dipole moment at the same frequency in the molecule. This dipole emits, according to the classical electromagnetic theory, at the same wavelength. For incident natural radiation, the radiation scattered at $\Theta = 90°$ must be completely polarized, with vibrations of the electric field vector perpendicular to the scattering plane. However, this theoretical prediction has not been confirmed by observations revealing a small depolarization at 90°. Later on, a correction for the molecular anisotropy was introduced by Cabannes (1929) in order to explain why the degree of polarization is not 100% at $\Theta = 90°$. The depolarization factor d is defined as the ratio of the parallel to the perpendicular components of the electric field vector at $\Theta = 90°$. It has been measured several times, but is still subject to uncertainty, leading to an uncertainty of about 2% in the so-called King factor $(6+3d)/(6-7d)$ appearing in Eq. (2.33) below.

The molecular scattering coefficient for dry air is

$$\sigma_{s,R} = \frac{24\pi^3}{\lambda^4}\left(\frac{m_s^2 - 1}{m_s^2 + 2}\right)^2 \frac{6 + 3d}{6 - 7d}\frac{N}{N_s^2}, \tag{2.33}$$

where $\lambda = 2\pi/k$ is the wavelength, $k = |\mathbf{k}|$ is the wave number, m_s is the refractive index for standard air (defined as dry air containing 0.03% CO_2 at a pressure of 1013.25 hPa and a temperature of 15°C), N is the molecular density, and N_s is the same quantity in standard conditions. The m_s is also subject to some uncertainty and slightly depends on the wavelength. Bodhaine et al. (1999) carefully analyzed the data available for computing the molecular scattering coefficient and their uncertainties. They proposed the following best-fit equation for the Rayleigh scattering cross section defined, as above, by $C_{s,R} = \sigma_{s,R}/N$:

$$C_{s,R}(\times 10^{-28}\text{cm}^2) = \frac{1.0455996 - 341.29061\lambda^{-2} - 0.90230850\lambda^2}{1 + 0.0027059889\lambda^{-2} - 85.968563\lambda^2}. \tag{2.34}$$

The corresponding Rayleigh scattering matrix is as follows:

$$\mathbf{F}_R(\Theta) = K\begin{bmatrix} \frac{3}{4}(1+\cos^2\Theta) & -\frac{3}{4}\sin^2\Theta & 0 & 0 \\ -\frac{3}{4}\sin^2\Theta & \frac{3}{4}(1+\cos^2\Theta) & 0 & 0 \\ 0 & 0 & \frac{3}{2}\cos\Theta & 0 \\ 0 & 0 & 0 & K'\frac{3}{2}\cos\Theta \end{bmatrix} + (1-K)\begin{bmatrix} 1 & 0 & 0 & 0 \\ 0 & 0 & 0 & 0 \\ 0 & 0 & 0 & 0 \\ 0 & 0 & 0 & 0 \end{bmatrix}, \tag{2.35}$$

where

$$K = \frac{1-d}{1+d/2}, \tag{2.36}$$

$$K' = \frac{1-2d}{1-d}. \tag{2.37}$$

2.6 Lorenz–Mie theory

The complete theory of electromagnetic scattering by an individual spherical particle was first presented by Gustav Mie (Mie, 1908; see Mishchenko and Travis, 2008 for a historical perspective on this seminal development). Detailed accounts of the Lorenz–Mie theory can be found in Stratton (1941), van de Hulst (1957), Bohren and Huffman (1983), and Lenoble (1993). The incident electromagnetic field is expressed as a linear combination of elementary solutions of the vector wave equation in spherical coordinates called vector spherical wave functions (VSWFs). The scattered and internal fields are expressed similarly, with unknown coefficients being obtained from the boundary conditions at the particle surface.

Consider an isolated homogeneous spherical particle, having a radius r, illuminated by a plane electromagnetic wave, as defined in Section 2.4.1. Using the scattering plane for reference (Figures 2.4 and 2.5), the scattered field vector components at a large distance ρ from the particle (i.e., in the so-called far-field zone; see Section 3.2 of Mishchenko et al., 2006) are given by

$$E_{sl} = \frac{i}{k\rho}\exp(-ik\rho)S_2(\Theta)E_{0l}, \tag{2.38a}$$

$$E_{sr} = \frac{i}{k\rho}\exp(-ik\rho)S_1(\Theta)E_{0r}, \tag{2.38b}$$

where S_1 and S_2 are complex functions of the scattering angle given by the following series:

$$S_1(\Theta) = \sum_{n=1}^{n_{max}} \frac{2n+1}{n(n+1)}\left(a_n \frac{d}{d\Theta}P_n^1(\cos\Theta) + b_n \frac{1}{\sin\Theta}P_n^1(\cos\Theta)\right), \tag{2.39a}$$

$$S_2(\Theta) = \sum_{n=1}^{n_{max}} \frac{2n+1}{n(n+1)}\left(b_n \frac{d}{d\Theta}P_n^1(\cos\Theta) + a_n \frac{1}{\sin\Theta}P_n^1(\cos\Theta)\right). \tag{2.39b}$$

The so-called Mie coefficients a_n correspond to magnetic oscillations, while the b_n correspond to electric oscillations. They are determined from the boundary conditions at the particle surface and depend on the complex refractive index of the particle relative to the surrounding medium m and on the particle size parameter $x = kr$.

The number of numerically significant terms n_{max} in the series (2.39) is of the order of $2x+3$; the same number is necessary in the expansions (2.31). Therefore, the practical application of the Lorenz–Mie theory for particles larger than the wavelength was delayed until the advent of modern computers. At present, several numerically efficient and highly accurate Lorenz–Mie codes are publicly available on the Internet (see, e.g., ftp://ftp.giss.nasa.gov/pub/crmim/spher.f).

From Eqs (2.38) and the definition of the Stokes parameters, it is straightforward to show that the non-zero elements of the normalized Lorenz–Mie scattering matrix are as follows:

$$F_{11}(\Theta) = F_{22}(\Theta) = p(\Theta) = \frac{\lambda^2}{2\pi C_s}[S_1(\Theta)S_1^*(\Theta) + S_2(\Theta)S_2^*(\Theta)], \tag{2.40a}$$

$$F_{21}(\Theta) = F_{12}(\Theta) = \frac{\lambda^2}{2\pi C_s}[S_2(\Theta)S_2^*(\Theta) - S_1(\Theta)S_1^*(\Theta)], \tag{2.40b}$$

$$F_{33}(\Theta) = F_{44}(\Theta) = \frac{\lambda^2}{2\pi C_s}[S_2(\Theta)S_1^*(\Theta) + S_1(\Theta)S_2^*(\Theta)], \tag{2.40c}$$

$$F_{34}(\Theta) = -F_{43}(\Theta) = \frac{i\lambda^2}{2\pi C_s}[S_1(\Theta)S_2^*(\Theta) - S_2(\Theta)S_1^*(\Theta)], \tag{2.40d}$$

where C_s is the corresponding scattering cross section. The latter is often expressed in terms of the scattering efficiency factor Q_s as follows:

$$C_s = \pi r^2 Q_s, \tag{2.41}$$

with

$$Q_s = \frac{2}{x^2} \sum_{n=1}^{n_{max}} (2n+1)(|a_n|^2 + |b_n|^2). \tag{2.42}$$

Similarly, the extinction cross section is represented as

$$C_e = \pi r^2 Q_e, \tag{2.43}$$

while the extinction efficiency factor is given by

$$Q_e = \frac{2}{x^2} \sum_{n=1}^{n_{max}} (2n+1)\,\mathrm{Re}(a_n + b_n), \tag{2.44}$$

where, as before, Re stands for the real part. If the particle absorbs radiation (i.e., the relative refractive index m has a non-zero imaginary part) then the extinction cross section is greater than the scattering cross section; otherwise they are equal. The extinction and scattering efficiencies are examples of dimensionless scale-invariant quantities depending only on the ratio of the particle size to the wavelength rather than on r and λ separately provided that the relative refractive index m is wavelength-independent (see Section 3.5 of Mishchenko et al., 2006). The normalized Stokes scattering matrix **F** defined by Eq. (2.23) is another scale-invariant quantity.

For a polydisperse ensemble of spherical particles, the average scattering and the extinction cross sections are given by

$$C_s = \int_0^\infty \pi r^2 Q_s(x, m) n(r) dr, \tag{2.45a}$$

$$C_e = \int_0^\infty \pi r^2 Q_e(x, m) n(r) dr, \tag{2.45b}$$

where $n(r)dr$ is the fraction of particles with radii between r and $r+dr$ normalized such that

$$\int_0^\infty n(r) dr = 1. \tag{2.46}$$

The corresponding formula for the ensemble-averaged elements of the normalized scattering matrix is as follows:

$$F_{ij}(\Theta) = \frac{1}{C_s}\int_0^\infty \pi r^2 Q_s(x, m)n(r)F_{ij}(\Theta; x, m)dr. \tag{2.47}$$

2.7 Nonspherical particles: Theory and measurements

Although spherical (or nearly spherical) aerosols do exist (e.g., Figure 2.6a), many aerosol types exhibit complex particle morphologies (e.g., Figures 2.6b–d), thereby rendering the Lorenz–Mie theory potentially inapplicable. The optical properties of such nonspherical and/or heterogeneous particles must be either computed using an advanced theory of elec-

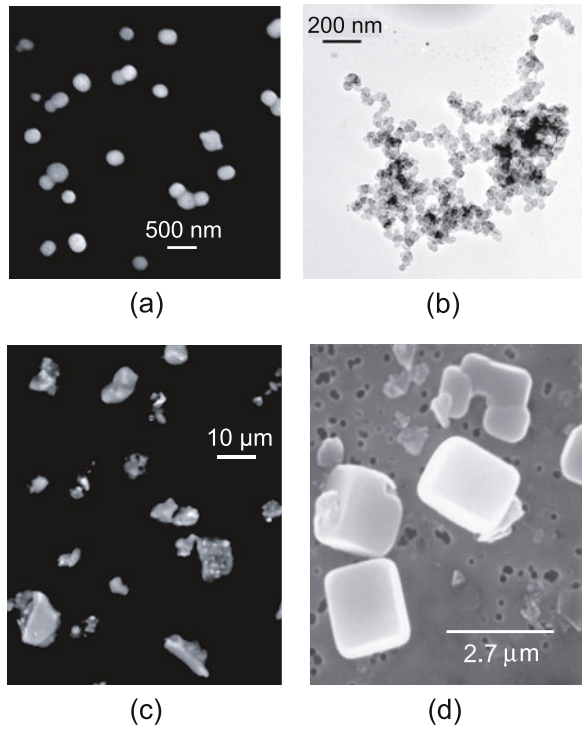

Figure 2.6 Examples of aerosol-particle morphologies. (a) Sub-micrometer-sized quasi-spherical ammonium sulphate and dust aerosols (after Weinzierl et al., 2009). (b) A soot aggregate (after Li et al., 2003). (c) Sahara-desert soil particles (after Weinzierl et al., 2009). (d) Dry sea-salt particles (after Chamaillard et al., 2003).

tromagnetic scattering or measured experimentally, both approaches having their strengths, weaknesses, and limitations. In this section, we provide a brief summary of the existing theoretical and experimental techniques for the determination of single-particle scattering and absorption characteristics. Detailed information and further references can be found in the books by Mishchenko et al. (2000, 2002) and Babenko et al. (2003) as well as in the review by Kahnert (2003).

2.7.1 Numerically-exact and approximate theoretical techniques

The majority of the existing exact theoretical approaches belong to one of two broad categories. Specifically, differential equation methods yield the scattered field via the solution of the Maxwell equations or the vector wave equation in the frequency or in the time domain, whereas integral equation methods are based on the volume or surface integral counterparts of the Maxwell equations.

The classical example of a differential equation method is the Lorenz–Mie theory discussed in the preceding section. By implementing a recursive procedure, one can generalize the Lorenz–Mie solution to deal with concentric multilayer spheres.

Like the Lorenz–Mie theory, the separation of variables method (SVM) for homogeneous or layered spheroids is a frequency-domain technique, wherein all fields and sources are assumed to vary in time according to the same factor $\exp(i\omega t)$. The SVM is based on solving the electromagnetic scattering problem in spheroidal coordinates by means of expanding the incident, internal, and scattered fields in appropriate vector spheroidal wave functions. The expansion coefficients of the incident field can be computed analytically, whereas the unknown expansion coefficients of the internal and scattered fields are determined by applying the appropriate boundary conditions. Unfortunately, the vector spheroidal wave functions are not orthogonal on the surface of a spheroid. Therefore, this procedure yields an infinite set of linear algebraic equations for the unknown coefficients which has to be truncated and solved numerically. The main limitation of the SVM is that it can be applied only to spheroidal scatterers, whereas its primary advantages are the applicability to spheroids with extreme aspect ratios and the ability to produce accurate benchmarks.

Another frequency-domain differential equation technique is the finite element method (FEM) which yields the scattered field via solving numerically the vector Helmholtz equation subject to the standard boundary conditions. The scattering object is intentionally imbedded in a finite computational domain, the latter being discretized into many cells with about 10 to 20 cells per wavelength. The electric field values are specified at the nodes of the cells and are initially unknown. Using the boundary conditions, the differential equation is converted into a matrix equation for the unknown node field values. The latter is solved using the standard Gaussian elimination or one of the preconditioned iterative techniques such as the conjugate gradient method. While scattering in the far-field zone is an open-space problem, the FEM is always implemented in a finite computational domain in order to limit the number of unknowns. Therefore, one has to impose approximate absorbing boundary conditions at the outer boundary of the computational domain, thereby suppressing wave reflections back into the computational domain and allowing the numerical analogs of the outward-propagating wave to exit the domain almost as if the domain were infinite. In principle, the FEM can be applied to arbitrarily shaped and inhomogeneous

particles and is simple in terms of its concept and practical implementation. However, FEM computations are spread over the entire computational domain rather than confined to the scatterer itself. This makes the technique rather slow and limits particle size parameters to values less than about 15. The finite spatial discretization and the approximate absorbing boundary conditions limit the accuracy of the method.

Unlike the frequency-domain FEM, the finite difference time domain method (FDTDM) yields the solution of the electromagnetic scattering problem in the time domain by directly solving the Maxwell time-dependent curl equations (e.g., Taflove and Hagness, 2000; P. Yang et al., 2000). The space and time derivatives of the electric and magnetic fields are approximated using a finite difference scheme with space and time discretizations selected so that they constrain computational errors and ensure numerical stability of the algorithm. As before, the scattering object must be imbedded in a finite computational domain, which requires the imposition of absorbing boundary conditions as a model of scattering in the open space. Representing a scattering object with curved boundaries using rectangular grid cells causes a staircasing effect and increases numerical errors, especially for particles with large relative refractive indices. Since the FDTDM yields the near field in the time domain, a special near-zone to far-zone transformation must be implemented in order to compute the requisite scattered far field in the frequency domain. The FDTDM has the same advantages as the FEM and shares its limitations in terms of accuracy and size parameter range.

The interaction of an incident plane electromagnetic wave with an arbitrary particle can also be described fully by the frequency-domain so-called volume integral equation (VIE). The calculation of the scattered field using the VIE would be straightforward except that the internal electric field entering the integrand is unknown beforehand. Therefore, the VIE must first be solved for the internal field. The integral over the particle volume is approximated by partitioning the interior region into a large number N of small cubical cells with about 10 to 20 cells per wavelength and assuming that the electric field and the refractive index within each cell are constant. The resulting system of N linear algebraic equations for the N unknown internal fields is solved numerically. Once the internal fields are found, the scattered field is determined by evaluating the right-hand side of the original VIE. This version of the VIE method is known as the method of moments (MOM). The simple approach to solving the MOM matrix equation for the internal fields by using the standard Gaussian elimination is not practical for particle size parameters exceeding unity. The conjugate gradient method together with the fast Fourier transform can be applied to significantly larger size parameters and reduces computer memory requirements substantially. The traditional drawback of using a preconditioned iterative technique is that computations must be repeated anew for each illumination direction.

Another version of the VIE technique is the so-called discrete dipole approximation (DDA). Whereas the MOM deals with the *actual* electric field in the center of each cell, the DDA exploits the concept of *exciting* fields and is based on discretizing the particle into a number N of elementary polarizable units called dipoles. The form of the electromagnetic response of each dipole to the local exciting electric field is assumed to be known. The field exciting a dipole is a superposition of the external (incident) field and the partial fields scattered by all the other dipoles. This allows one to form a system of N linear equations for the N fields exciting the N dipoles. The numerical solution of the DDA matrix equation is then used to compute the N partial fields scattered by the dipoles and thus the total scat-

tered field. The original formulation of the DDA in the mid-1970s was phenomenological; however, it has been demonstrated since that the DDA can be derived from the VIE and thus is closely related to the MOM.

The main advantages of the MOM and the DDA are that they automatically satisfy the asymptotic radiation condition at infinity and can be applied to inhomogeneous, anisotropic, and optically active scatterers. Furthermore, the actual computation is confined to the scatterer volume, thereby resulting in fewer unknowns than the differential equation methods. However, the numerical accuracy of the MOM and DDA is relatively low and improves rather slowly with increasing N, whereas the computer time grows rapidly with increasing size parameter. Another disadvantage of these techniques is the need to repeat the entire calculation for each new direction of incidence. Further information on the MOM and the DDA and their applications can be found in the recent review by Yurkin and Hoekstra (2007).

The classical Lorenz–Mie solution can be extended to a cluster of non-overlapping spheres by using the translation addition theorem for the participating VSWFs. The total field scattered by the multisphere cluster is represented as a superposition of individual (partial) fields scattered by each sphere. The external electric field illuminating the cluster and the individual fields scattered by the constituent spheres are expanded in VSWFs with origins at the individual sphere centers. The orthogonality of the VSWFs in the sphere boundary conditions is exploited by applying the translation addition theorem wherein a VSWF centered at one sphere origin is re-expanded about another sphere origin. This procedure ultimately results in a matrix equation for the scattered-field expansion coefficients of each sphere. A numerical computer solution of this equation for the specific incident field yields the partial scattered fields and thereby the total scattered field.

Alternatively, the numerical inversion of the cluster matrix equation yields sphere-centered transition matrices (or T matrices) that transform the expansion coefficients of the incident field into the expansion coefficients of the individual scattered fields. In the far-field region of the entire cluster, the individual scattered-field expansions can be transformed into a single expansion centered at a single origin inside the cluster. This procedure yields the cluster T matrix transforming the incident-wave expansion coefficients into the single-origin expansion coefficients of the total scattered field and can be used in the highly efficient semi-analytical averaging of scattering characteristics over cluster orientations (Mackowski and Mishchenko, 1996).

This so-called superposition method (SM) has been extended to spheres with one or more eccentrically positioned spherical inclusions as well as to clusters of spheroids in an arbitrary configuration. Owing to the analyticity of its mathematical formulation, the SM is capable of producing very accurate numerical results.

The T-matrix method (TMM) is based on the expansion of the incident field in VSWFs regular at the origin of the coordinate system and on the expansion of the scattered field outside a circumscribing sphere of the scatterer in VSWFs regular at infinity. The T matrix transforms the expansion coefficients of the incident field into those of the scattered field and, if known, can be used to compute any scattering characteristic of the particle. The TMM was initially developed by Waterman (1971) for single homogeneous objects, but has since been generalized to deal with multilayered scatterers and arbitrary clusters of nonspherical particles. For a homogeneous or concentrically layered sphere, all TMM formulas reduce to

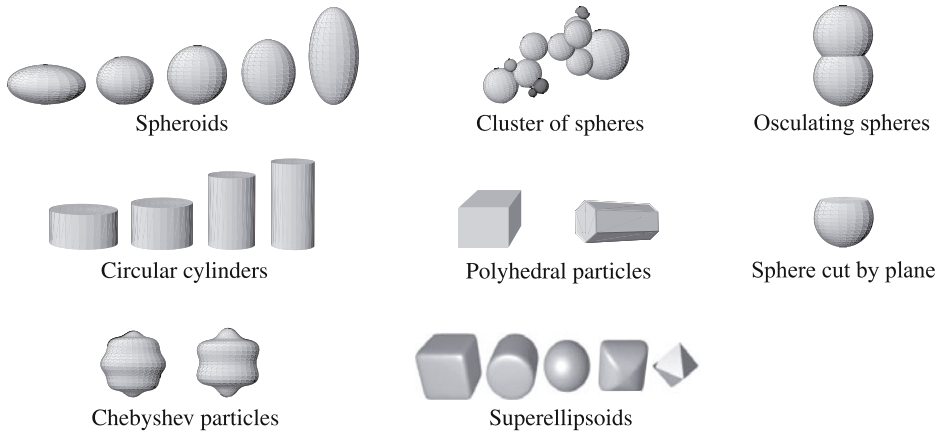

Figure 2.7 Types of particles that can be treated with the *T*-matrix method.

those of the Lorenz–Mie theory. In the case of a cluster composed of spherical components, the TMM reduces to the multisphere SM mentioned above.

The *T* matrix for single homogeneous and multilayered scatterers is usually computed using the so-called extended boundary condition method (EBCM) applicable to any particle shape, although computations become much simpler and much more efficient for bodies of revolution. Special procedures have been developed to improve the numerical stability of EBCM computations for large size parameters and/or extreme aspect ratios. More recent work has demonstrated the practical applicability of the EBCM to particles without axial symmetry, e.g., ellipsoids, cubes, and finite polyhedral cylinders. The computation of the *T* matrix for a cluster of particles is based on the assumption that the *T* matrices of all components are known and is based on the use of the translation addition theorem for the VSWFs.

The loss of efficiency for particles with large aspect ratios or with shapes lacking axial symmetry is the main drawback of the TMM. The main advantages of the TMM are high accuracy and speed coupled with applicability to particles with equivalent-sphere size parameters exceeding 200. There are several semi-analytical orientation averaging procedures that make TMM computations for randomly oriented particles as fast as those for a particle in a fixed orientation.

Figure 2.7 shows examples of particles that can be treated using various implementations of the TMM. A representative collection of public-domain *T*-matrix computer programs has been available at http://www.giss.nasa.gov/staff/mmishchenko/t_matrix.html since 1996 and has been used in more than 780 peer-reviewed publications. These programs have been developed specifically to deal with axially symmetric particles and clusters of spherical monomers. Typical examples are spheroids, finite circular cylinders, Chebyshev particles

(Wiscombe and Mugnai, 1986), osculating spheres, spheres cut by a plane, and clusters of spherical particles with touching or separated components. In all cases, the scattering object in question can be randomly or preferentially oriented. The EBCM-based programs have been thoroughly tested against the SVM for spheroids. The very high numerical accuracy of the *T*-matrix codes has been used to generate benchmark results with five and more accurate decimals which can be used for testing other numerically-exact and approximate approaches. Extensive timing tests have shown that the numerical efficiency of these *T*-matrix codes is unparalleled, especially in computations for randomly oriented particles.

The SVM, SM, and TMM are the only methods that can yield very accurate results for particles comparable to and larger than a wavelength. The analytical orientation averaging procedure makes the TMM the most efficient technique for randomly oriented particles with moderate aspect ratios. Particles with larger aspect ratios can be treated with the SVM and an iterative EBCM. Computations for anisotropic objects and homogeneous and inhomogeneous particles lacking rotational symmetry often have to rely on more flexible techniques such as the FEM, FDTDM, MOM, and DDA. All these techniques are conceptually simple, can be easily implemented, and have comparable performance characteristics. However, their simplicity and flexibility are often accompanied by lower efficiency and accuracy and by stricter practical limitations on the range of size parameters and/or refractive indices. A comprehensive collection of computer programs based on various exact numerical techniques is available at http://www.scattport.org/.

The practical importance of approximate theories of electromagnetic scattering diminishes as computers become more efficient while numerically-exact techniques mature and become applicable to a wider range of problems. However, at least one approximation, the geometrical optics method (GOM), is not likely to become obsolete in the near future since its accuracy often improves as the particle size parameter grows, whereas all numerically-exact theoretical techniques for nonspherical particles become inapplicable whenever the size parameter exceeds a certain threshold. The GOM is a phenomenological approach to the computation of electromagnetic scattering by an arbitrarily shaped particle with a size much greater than the wavelength of the incident light. It is based on the assumption that the incident plane wave can be represented as a collection of "independent (or incoherent) parallel rays". The history of each ray impinging on the particle boundary is traced individually using Snell's law and Fresnel's formulas. Each incident ray is partially reflected and partially refracted into the particle. The refracted ray may emerge after an inside–out refraction, possibly preceded by one or more internal reflections, and can be attenuated by absorption inside the particle. Each internal ray is traced until its intensity decreases below a prescribed cutoff value. Varying the polarization state of the incident rays, sampling all emerging rays into predefined narrow angular bins, and adding "incoherently" the respective Stokes parameters of the emerging rays yields a quantitative representation of the particle's scattering properties in terms of the ray-tracing scattering matrix. The ray-tracing extinction cross section does not depend on the polarization state of the incident light and is equal to the geometrical area *G* of the particle projection on the plane perpendicular to the incidence direction. The presence of the particle modifies the incident plane wave front by eliminating a part that has the shape and size of the geometrical projection of the particle. Therefore, the ray-tracing scattering pattern is artificially supplemented by adding the Fraunhofer pattern caused by diffraction of the incident wave on the particle projection.

Since the particle size is assumed to be much greater than the incident wavelength, the diffraction component of the scattering matrix is confined to a narrow angular cone centered at the exact forward-scattering direction.

The main advantage of the GOM is its applicability to essentially any particle shape. However, this technique is approximate by definition, which implies that its range of applicability in terms of the smallest size parameter must be examined thoroughly by comparing GOM results with numerically-exact solutions of the Maxwell equations. Such comparisons with Lorenz–Mie and *T*-matrix results have demonstrated that although the main geometrical optics features can be reproduced qualitatively by particles with size parameters less than 100, obtaining good quantitative accuracy in GOM computations of the scattering matrix requires size parameters exceeding a few hundred. Even then, the GOM fails to reproduce scattering features caused by various interference effects.

The so-called physical optics or Kirchhoff approximation (KA) has been developed with the purpose of improving the GOM performance (see, e.g., P. Yang and Liou, 2006). This technique is based on expressing the scattered field in terms of the electric and magnetic fields on the exterior side of the particle boundary. The latter are computed approximately using Fresnel's formulas and the standard ray-tracing procedure. The KA partially preserves the phase information and reproduces some physical optics effects ignored completely by the simple GOM.

2.7.2 Measurement techniques

The majority of existing laboratory measurement techniques fall into two basic categories:

- scattering of visible or infrared light by particles with sizes from several hundredths of a micron to several hundred microns;
- scattering of microwaves by millimeter- and centimeter-sized objects.

Measurements in the visible and infrared parts of the spectrum benefit from the availability of sensitive detectors of electromagnetic energy, diverse sources of radiation, and high-quality optical elements. They usually involve less expensive and more portable instrumentation and can be performed in the field as well as in the laboratory. However, they may be more difficult to interpret due to lack of independent information on sample microphysical characteristics and composition. Microwave scattering experiments often require more cumbersome and expensive instrumentation and large stationary measurement facilities, but allow almost full control over the scattering object.

Traditional detectors of electromagnetic energy in the visible and near-infrared spectral regions are polarization-insensitive, which means that the detector response is determined only by the first Stokes parameter of the radiation impinging on the detector. This implies that in order to measure all 16 elements of the scattering matrix, one must use optical elements that can vary the polarization state of light before and after scattering in a specific and controllable way. Figure 2.8 depicts the scheme of a modern laboratory setup used to measure the scattering matrix for a small group of natural or artificial particles. The laser beam first passes through a linear polarizer and a polarization modulator and then illuminates particles contained in the scattering chamber. Light scattered by the particles at an

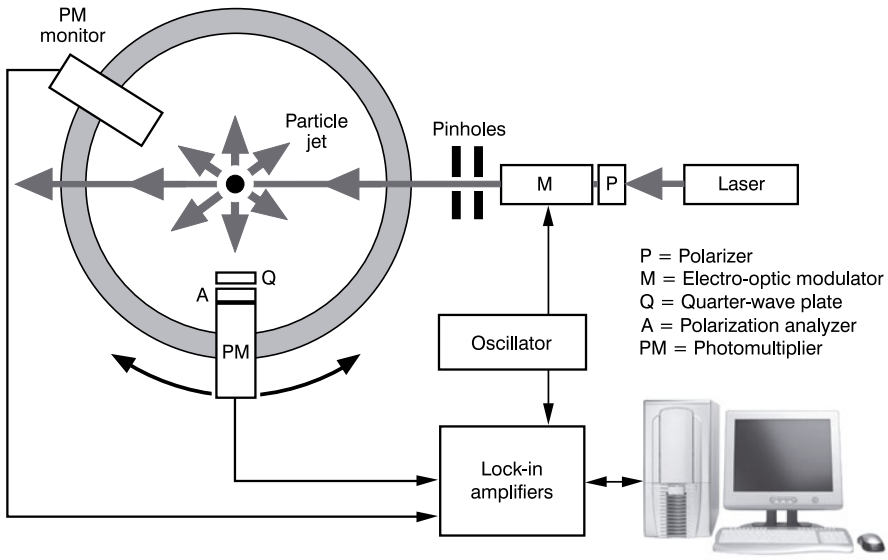

Figure 2.8 Schematic view of a laboratory scattering setup based on measurements of visible or near-infrared light (after Hovenier, 2000).

angle Θ relative to the incidence direction passes a quarter-wave plate and a polarization analyzer, after which its intensity is measured by a detector. The transformation Mueller matrices of the polarizer, modulator, quarter-wave plate, and analyzer depend on their orientation with respect to the scattering plane and can be varied precisely. Because the detector measures only the first element of the resulting Stokes column vector, several measurements with different orientations of the optical components with respect to the scattering plane are necessary for the full determination of the scattering matrix. This procedure must be repeated at different scattering angles in order to determine the full angular profile of the scattering matrix, perhaps with the exception of near-forward and/or near-backward directions. This laboratory technique has been used to accumulate a large and representative set of scattering-matrix data for samples of natural and artificial aerosols (see, e.g., the review by Muñoz and Volten, 2006 and references therein)

In accordance with the above-mentioned electromagnetic scale invariance rule (see Section 3.5 of Mishchenko et al., 2006), the main idea of the microwave analog technique is to manufacture a centimeter-sized scattering object with desired shape and refractive index, measure the scattering of a microwave beam by this object, and finally extrapolate the result to visible or near-infrared wavelengths by keeping the ratio of the object size to the wavelength fixed. In a modern microwave scattering setup (e.g., Gustafson, 2009), radiation from a transmitting conical horn antenna passes through a collimating lens and a

polarizer. The lens produces a nearly flat wave front which is scattered by an analog particle model. The scattered wave passes through another polarizer and lens and is measured by a receiving horn antenna. Positioning the receiver end of the setup at different scattering angles yields information on the angular distribution of the scattered radiation. By varying the orientations of the two polarizers, one can measure all 16 elements of the scattering matrix.

2.8 Illustrative theoretical and laboratory results

The review by Hansen and Travis (1974) and monographs by Mishchenko et al. (2000, 2002) provide a detailed discussion of extinction, scattering, and absorption properties of aerosol particles having diverse morphologies and compositions. Plentiful information on light scattering by nonspherical and morphologically complex particles can also be found in several special issues of the Journal of Quantitative Spectroscopy and Radiative Transfer (Hovenier, 1996; Lumme, 1998; Mishchenko et al., 1999b, 2008; Videen et al., 2001, 2004; Kolokolova et al., 2003; Wriedt, 2004; Moreno et al., 2006; Voshchinnikov and Videen, 2007; Horvath, 2009; Hough, 2009). Therefore, the limited purpose of the several illustrative examples given in this section is to highlight the most typical traits of the single-scattering patterns caused by small particles.

Figure 2.9 shows the extinction efficiency factor defined by Eq. (2.43) versus size parameter x for monodisperse spheres with three real-valued relative refractive indices. Each curve exhibits a succession of major low-frequency maxima and minima with a superimposed high-frequency ripple consisting of sharp, irregularly spaced extrema many of which are super-narrow spike-like features. The major maxima and minima are called the "interference structure" since they are usually interpreted as being the result of interference of light diffracted and transmitted by the particle. Unlike the interference structure, the so-called morphology-dependent resonances (MDRs) forming the ripple are caused by the resonance behavior of the Lorenz–Mie coefficients a_n and b_n at specific size-parameter values. The interference structure and the MDRs are typical attributes of all scattering characteristics of nonabsorbing monodisperse spheres.

Irrespective of m, the extinction efficiency rapidly vanishes in the Rayleigh domain of size parameters (i.e., as x approaches zero). Indeed, it is well known that for nonabsorbing particles much smaller than the wavelength,

$$Q_e \equiv Q_s \underset{x \to 0}{\propto} \frac{1}{\lambda^4}, \tag{2.48}$$

as first demonstrated by Lord Rayleigh and hence called Rayleigh scattering. As the particle size becomes much greater than the wavelength, Q_e tends to the asymptotic geometrical-optics value 2, with equal contributions from the rays striking the particle surface and the light diffracted by the particle projection. Figure 2.9 also demonstrates that for nonabsorbing particles with size parameters of order one, the extinction cross section can exceed

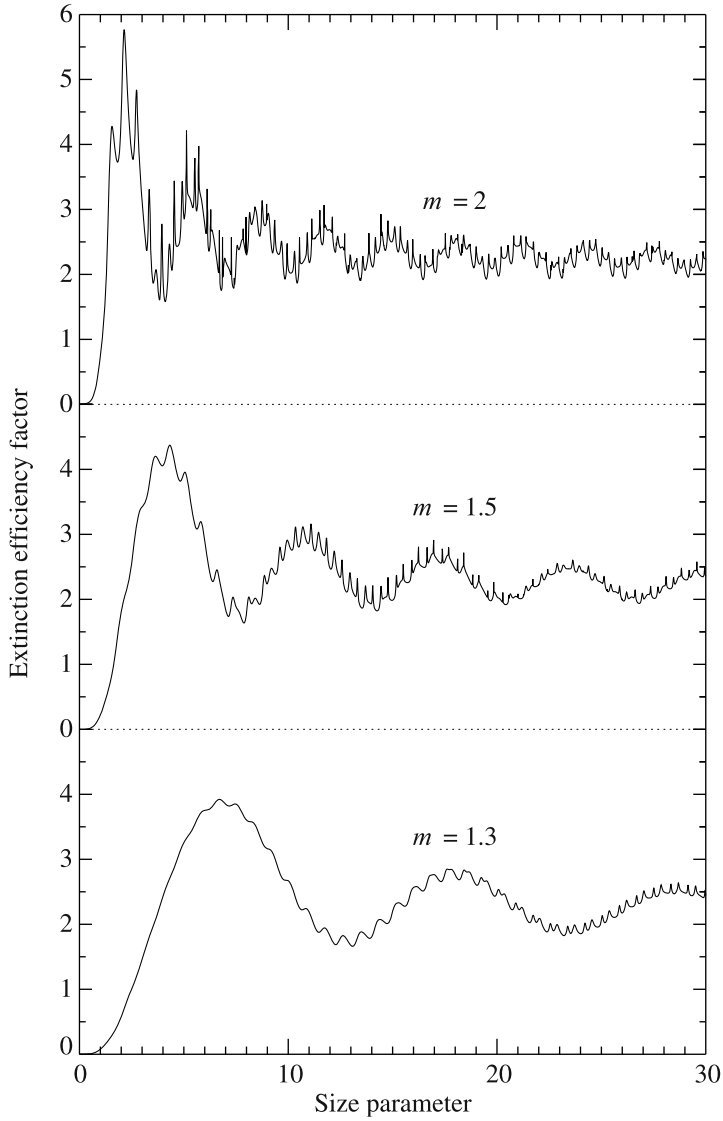

Figure 2.9 Extinction efficiency factor Q_e versus size parameter x for monodisperse, homogeneous spherical particles with relative refractive indices m = 1.3, 1.5, and 2.

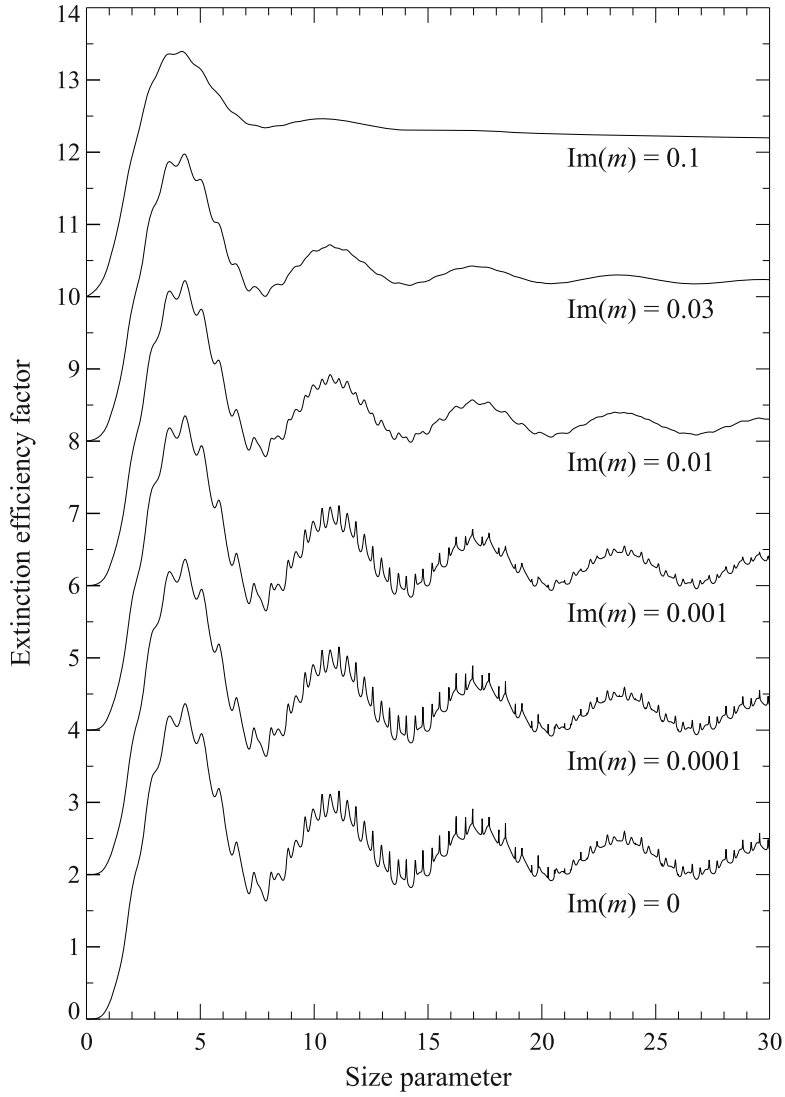

Figure 2.10 The effect of increasing absorption on the interference and ripple structures of the extinction efficiency factor for monodisperse spherical particles with the real part of the relative refractive index Re(m) = 1.5. The vertical axis scale applies to the curve with Im(m) = 0, the other curves being successively displaced upward by 2.

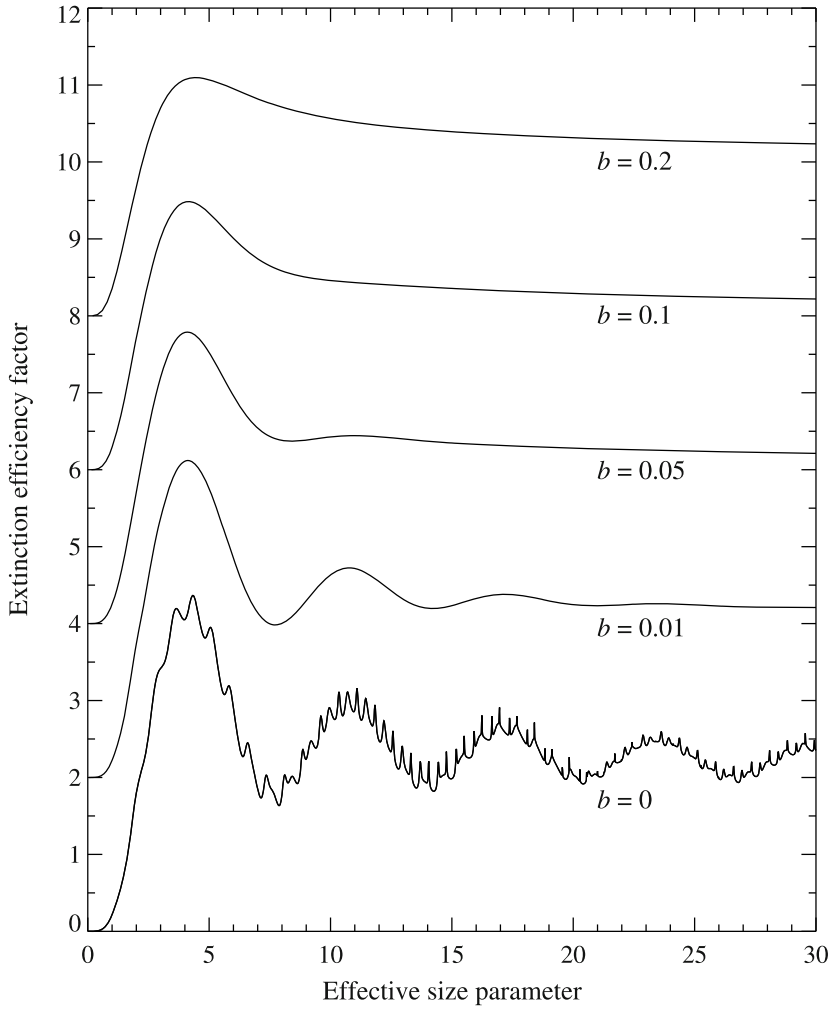

Figure 2.11 The effect of increasing width of the size distribution on the interference structure and ripple for nonabsorbing spherical particles with the real-valued relative refractive index $m = 1.5$ and effective size parameters x_{eff} ranging from 0 to 30. The vertical axis scale applies to the curve with $b = 0$, the other curves being successively displaced upward by 2.

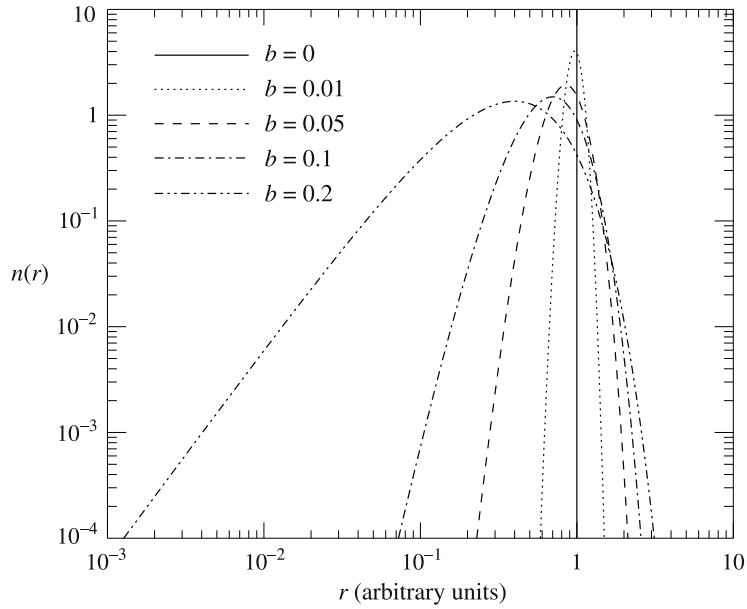

Figure 2.12 Gamma size distributions (2.50) with $a = 1$ (in arbitrary units of length) and $b = 0, 0.01, 0.05, 0.1$, and 0.2. The value $b = 0$ corresponds to monodisperse particles.

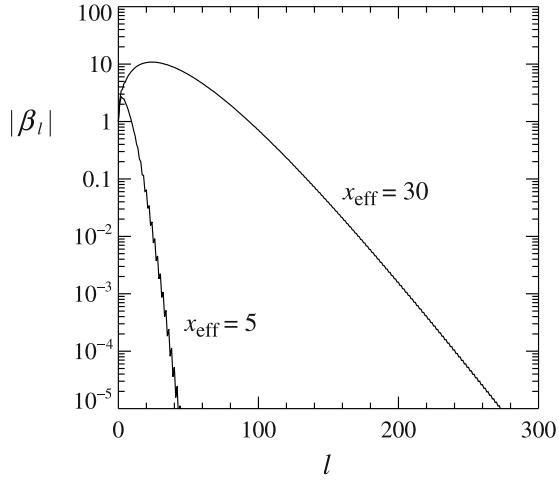

Figure 2.13 Expansion coefficients for two models of polydisperse spherical particles with effective size parameters $x_{\text{eff}} = 5$ and 30.

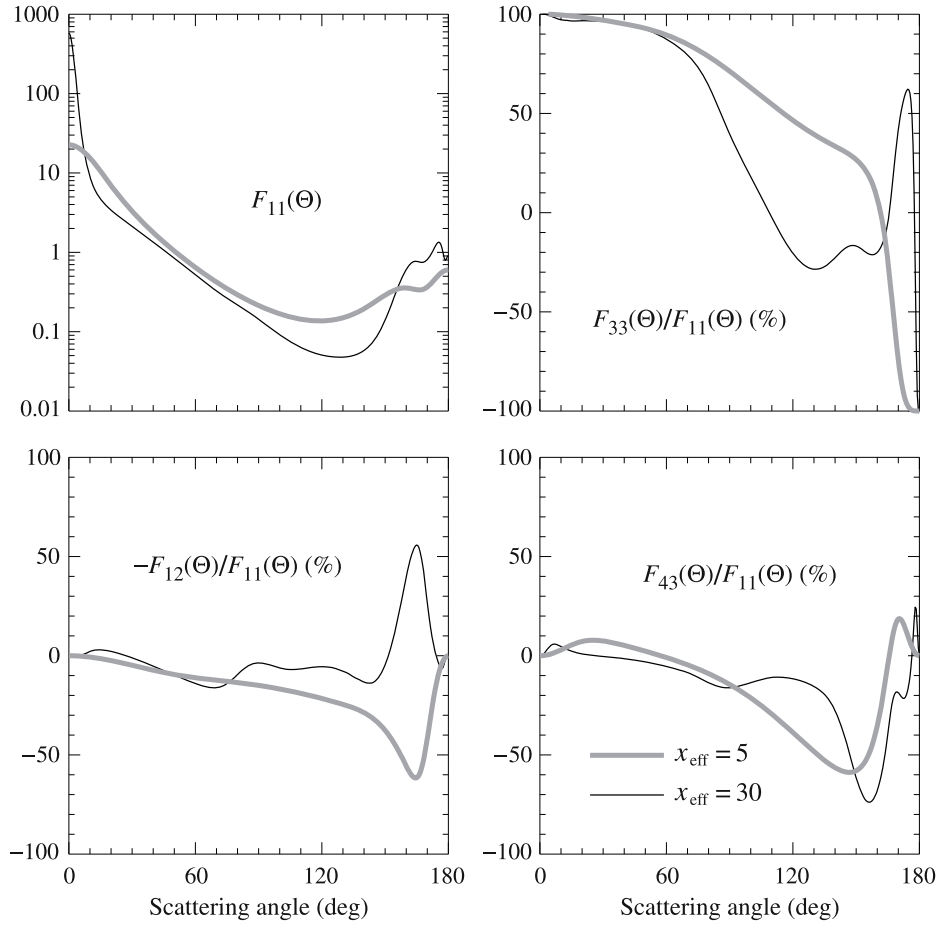

Figure 2.14 Elements of the normalized Stokes scattering matrix for two models of polydisperse spherical particles.

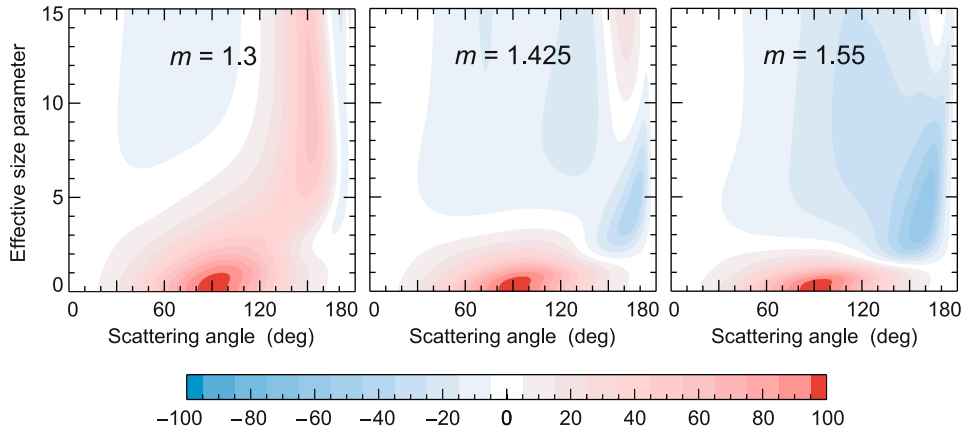

Figure 2.15 Degree of linear polarization for unpolarized incident light (in %) versus scattering angle Θ and effective size parameter ka for polydisperse spherical particles with relative refractive indices 1.3, 1.425, and 1.55. The effective variance of the gamma size distribution (2.50) is fixed at $b = 0.2$.

the particle geometrical cross section by more than a factor of 5.

For absorbing particles, extinction in the Rayleigh limit of size parameters is dominated by absorption and varies as the inverse wavelength:

$$Q_e \approx Q_a \underset{x \to 0}{\propto} \frac{1}{\lambda}. \tag{2.49}$$

The MDRs rapidly weaken and then vanish with increasing absorption, as Figure 2.10 demonstrates. Increasing the imaginary part of the relative refractive index $\mathrm{Im}(m)$ beyond 0.001 starts to affect and eventually suppresses most of the interference structure as well. However, the first interference maximum at $x \approx 4$ survives, although becomes significantly less pronounced, even at $\mathrm{Im}(m) = 0.1$.

A very similar smoothing effect on the interference structure and MDRs is caused by particle polydispersity. Figure 2.11 shows the results of Lorenz–Mie computations for the gamma distribution of particle radii

$$n(r) = \frac{1}{(ab)^{(1-2b)/b}\Gamma[(1-2b)/\mathrm{b}]} r^{(1-3b)/b} \exp\left(-\frac{r}{ab}\right), \quad r \in (0, \infty), \quad b \in [0, 5) \tag{2.50}$$

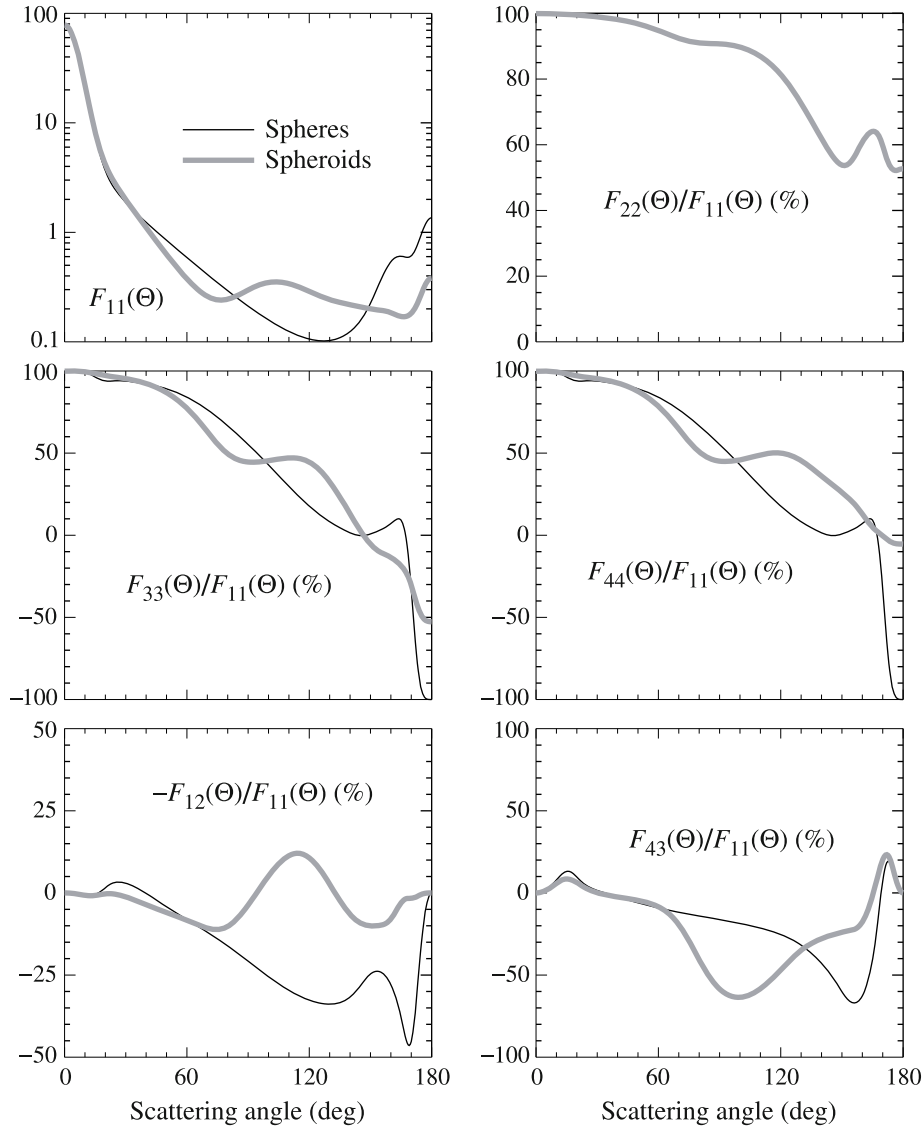

Figure 2.16 Elements of the normalized Stokes scattering matrix for the gamma distribution of spheres and surface-area-equivalent, randomly oriented oblate spheroids with $ka = 10$, $b = 0.1$, and $m = 1.53 + i0.008$. The ratio of the larger to the smaller spheroid axes is 2.

with the effective variance (width) b increasing from 0 (which corresponds to monodisperse particles) to 0.2 (which corresponds to a moderately wide size distribution). The efficiency factor is now defined as the average extinction cross section divided by the average area of the particle geometrical projection and is plotted against the effective size parameter defined as $x_{\text{eff}} = ka$. It is seen that increasing the width of the size distribution (see Figure 2.12) initially suppresses the MDRs and then eliminates the interference structure. Interestingly, as narrow a dispersion of sizes as that corresponding to $b = 0.01$ washes the MDRs out completely. The first major maximum of the interference structure persists to much larger values of b, but eventually fades away too.

To illustrate the dependence of the coefficients β_l entering the expansion (2.7) on particle physical characteristics, Figure 2.13 depicts them versus l for two polydispersions of spherical particles, each described by the gamma distribution (2.50). For both polydispersions, the relative refractive index is $m = 1.5$ and the effective variance is $b = 0.2$. The effective size parameter x_{eff} is equal to 5 for the first model and to 30 for the second model. Figure 2.14 visualizes the four non-zero independent elements of the normalized Stokes scattering matrix (2.29) for each polydispersion. Figure 2.13 reveals the typical behavior of the expansion coefficients β_l with increasing index l: they first grow in magnitude and then decay to absolute values below a meaningful numerical threshold. The greater the particle size parameter, the larger the maximal absolute value of the expansion coefficients and the slower their decay. This trend is largely explained by the rapid growth of the height of the forward-scattering peak in the phase function $p(\Theta) = F_{11}(\Theta)$ (as well as in the element $F_{33}(\Theta)$) with increasing x_{eff} (see Figure 2.14).

Besides the magnitude of the forward-scattering peak, the angular profiles of the two phase functions in Figure 2.14 are qualitatively similar. The same is largely true of the ratio $F_{43}(\Theta)/F_{11}(\Theta)$. On the other hand, the angular profiles of the ratios $F_{33}(\Theta)/F_{11}(\Theta)$ and $-F_{12}(\Theta)/F_{11}(\Theta)$ (the latter represents the degree of linear polarization of singly scattered light for unpolarized incident light) reveal a strong dependence on the effective size parameter. Indeed, at certain scattering angles these ratios can differ not just in magnitude but even in sign. Figure 2.15 demonstrates the equally strong dependence of the ratio $-F_{12}(\Theta)/F_{11}(\Theta)$ on the relative refractive index. These results illustrate well why measurements of polarization contain much more information on particle microphysics than measurements of intensity only (e.g., Mishchenko et al., 2010 and references therein).

The dependence of all scattering and absorption characteristics on particle microphysical properties can become much more intricate for nonspherical and/or morphologically complex particles, particularly those having a preferred orientation. This is especially true of the interference structure and MDRs, which now strongly depend on the particle orientation with respect to the incidence and scattering directions and on the polarization state of the incident light. However, averaging over orientations reinforces the effect of averaging over sizes and extinguishes many resonance features, thereby making scattering patterns for randomly oriented, polydisperse nonspherical particles even smoother than those for surface- or volume-equivalent polydisperse spheres. In fact, it is often difficult to distinguish spherical and randomly oriented nonspherical particles based on *qualitative* differences in their scattering patterns.

However, there can be significant *quantitative* differences in specific scattering patterns. As an example, Figure 2.16 contrasts the elements of the normalized Stokes scattering

matrix for polydisperse spheres and surface-equivalent, randomly oriented spheroids with a relative refractive index $m = 1.53 + i0.008$. The left-hand top diagram shows the corresponding phase functions and reveals the following five distinct scattering-angle ranges:

$$\begin{aligned}
&\text{nonsphere} \approx \text{sphere} \quad \text{from } \Theta = 0° \text{ to } \Theta \sim 15°–20°;\\
&\text{nonsphere} > \text{sphere} \quad \text{from } \Theta \sim 15°–20° \text{ to } \Theta \sim 35°;\\
&\text{nonsphere} < \text{sphere} \quad \text{from } \Theta \sim 35° \text{ to } \Theta \sim 85°;\\
&\text{nonsphere} \gg \text{sphere} \quad \text{from } \Theta \sim 85° \text{ to } \Theta \sim 150°;\\
&\text{nonsphere} \ll \text{sphere} \quad \text{from } \Theta \sim 150° \text{ to } \Theta = 180°.
\end{aligned} \tag{2.51}$$

Although the specific boundaries of these regions can be expected to shift with changing particle shape and relative refractive index, the enhanced side-scattering and suppressed backscattering appear to be rather typical characteristics of nonspherical particles.

The degree of linear polarization for unpolarized incident light, $-F_{12}(\Theta)/F_{11}(\Theta)$, tends to be positive at scattering angles around 120° for the spheroids, but is negative at most scattering angles for the surface-equivalent spheres. Whereas $F_{22}(\Theta)/F_{11}(\Theta) \equiv 1$ for spherical particles, the $F_{22}(\Theta)/F_{11}(\Theta)$ curve for the spheroids significantly deviates from 100% and causes a non-zero value of the linear depolarization ratio defined by

$$\delta_L = \frac{F_{11}(180°) - F_{22}(180°)}{F_{11}(180°) + F_{22}(180°)}. \tag{2.52}$$

Similarly, $F_{33}(\Theta)/F_{11}(\Theta) \equiv F_{44}(\Theta)/F_{11}(\Theta)$ for spherically symmetric particles, whereas the $F_{44}(\Theta)/F_{11}(\Theta)$ for the spheroids tends to be greater than the $F_{33}(\Theta)/F_{11}(\Theta)$ at most scattering angles, especially in the backscattering direction. The violation of the Lorenz–Mie equality $F_{44}(180°) = -F_{11}(180°)$ by the spheroids yields a non-zero value of the circular depolarization ratio defined by

$$\delta_C = \frac{F_{11}(180°) + F_{44}(180°)}{F_{11}(180°) - F_{44}(180°)} \equiv \frac{2\delta_L}{1-\delta_L} \tag{2.53}$$

(cf. Eq. (2.28)). The ratios $F_{43}(\Theta)/F_{11}(\Theta)$ for the spheres and the spheroids also reveal significant quantitative differences at scattering angles exceeding 60°. On the other hand, the nonspherical/spherical differences in the integral scattering and absorption characteristics are not nearly as significant as those in the scattering matrix elements.

Despite the significant progress in our ability to model scattering by nonspherical and morphologically complex particles, direct theoretical computations for many types of natural and artificial particles with sizes comparable to and greater than the wavelength (Figure 2.6) remain highly problematic. Therefore, there have been several attempts to simulate the scattering and absorption properties of actual particles using simple model shapes. These attempts have been based on the realization that in addition to size and orientation averaging, averaging over shapes can also be necessary in many cases. Indeed, usually ensembles

of natural and artificial particles exhibit a vast variety of shapes and morphologies, thereby making quite questionable the utility of a single model shape (however "irregular" it may look to the human eye) in the representation of scattering properties of an ensemble.

As an illustration, Figure 2.17 shows the phase functions computed for polydisperse, randomly oriented prolate spheroids with varying aspect ratios (Mishchenko et al., 1997). It is seen indeed that even after size and orientation averaging, each spheroidal shape produces a unique, aspect-ratio-specific angular scattering pattern, whereas laboratory and in situ measurements for real nonspherical particles usually show smooth and mostly featureless phase functions. On the other hand, the grey curves in Figure 2.18 (Dubovik et al., 2006) show that *shape mixtures* of polydisperse, randomly oriented prolate and oblate spheroids can provide a good quantitative fit to the results of accurate laboratory measurements of the scattering matrix for natural irregular particles. On the other hand, the Lorenz–Mie results depicted by black curves disagree with the laboratory data quite substantially.

These examples lead to two important conclusions. First of all, they provide evidence that the often observed smooth scattering-angle dependence of the elements of the scattering matrix for natural and artificial ensembles of nonspherical aerosols (e.g., Muñoz and Volten, 2006) is largely caused by the diversity of particle shapes in the ensemble. Secondly, they suggest that at least some scattering properties of ensembles of irregularly and randomly shaped aerosols can be modeled adequately using polydisperse shape mixtures of simple particles such as spheroids. It goes without saying that forming representative mixtures of less regular particles than spheroids should be expected to eventually provide an even better model of electromagnetic scattering by many natural and artificial aerosols (e.g., Bi et al., 2009; Zubko et al., 2009).

In most cases nonspherical–spherical differences in the optical cross-sections and the single-scattering albedo are much less significant than those in the scattering matrix elements. This does not mean, however, that the effects of nonsphericity and morphology on the integral scattering and absorption characteristics are always negligible or unimportant. An important type of particle characterized by integral radiometric properties substantially different from those of volume-equivalent spheres are clusters composed of large numbers of small monomers such as soot aggregates shown in Figure 2.6b (see, e.g., the reviews by Sorensen, 2001 and Moosmüller et al., 2009). The overall morphology of a dry soot aerosol is usually described by the following statistical scaling law:

$$N_{\rm S} = k_0 \left(\frac{R_{\rm g}}{a} \right)^{D_{\rm f}}, \tag{2.54}$$

where a is the monomer mean radius, k_0 is the prefactor, $D_{\rm f}$ is the fractal dimension, $N_{\rm S}$ is the number of spherical monomers in the cluster, and $R_{\rm g}$, called the radius of gyration, is a measure of the overall cluster radius. The fractal dimension is especially important for the quantitative characterization of the aggregate morphology. Densely packed aggregates have $D_{\rm f}$ values approaching 3, whereas the fractal dimension of chain-like branched clusters can be significantly smaller.

Detailed computations for fractal soot clusters based on the DDA and the superposition T-matrix method have been reported by Klusek et al. (2003), Liu and Mishchenko (2005,

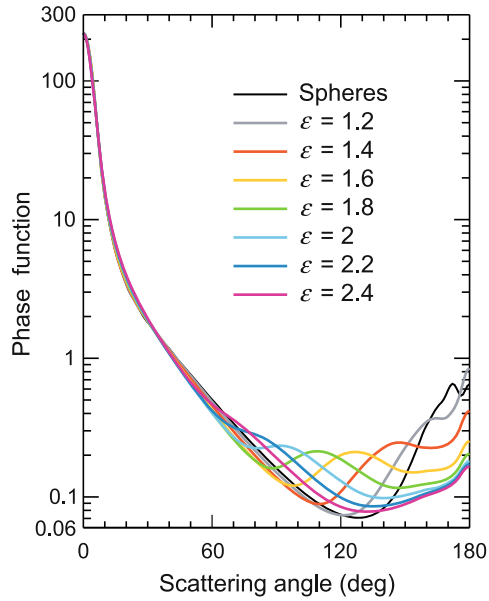

Figure 2.17 *T*-matrix computations of the phase function for micrometer-sized polydisperse spheres and randomly oriented surface-equivalent prolate spheroids with aspect ratios ε ranging from 1.2 to 2.4 at a wavelength of 443 nm. The relative refractive index is fixed at 1.53 + i0.008.

2007), Liu et al. (2008), and Kahnert (2010). These numerically exact results have demonstrated that the integral radiometric properties of the clusters can often be profoundly different from those of the volume-equivalent spheres. This is especially true of the scattering cross-section, single-scattering albedo, and the asymmetry parameter defined by Eq. (2.9).

Figure 2.19 depicts the results of *T*-matrix computations of the scattering matrix elements averaged over 20 soot-cluster realizations randomly computer-generated for the same values of the fractal parameters using the procedure developed by Mackowski (2006). In a rather peculiar way (cf. West, 1991), the angular scattering properties of the clusters appear to be a mix of those of wavelength-sized compact particles (the nearly isotropic Rayleigh phase function of the small individual spherules evolves into a forward scattering phase function) and Rayleigh scatterers (i.e., the ratio $-F_{12}(\Theta)/F_{11}(\Theta)$ is systematically positive, almost symmetric with respect to the scattering angle $\Theta = 90°$, and reaches a nearly 100% maximum at $\Theta \approx 90°$, while the ratio $F_{34}(\Theta)/F_{11}(\Theta)$ is very close to zero). The deviation of the ratio $F_{22}(\Theta)/F_{11}(\Theta)$ from 100% is the only unequivocal manifestation of the nonsphericity of the soot-cluster shape.

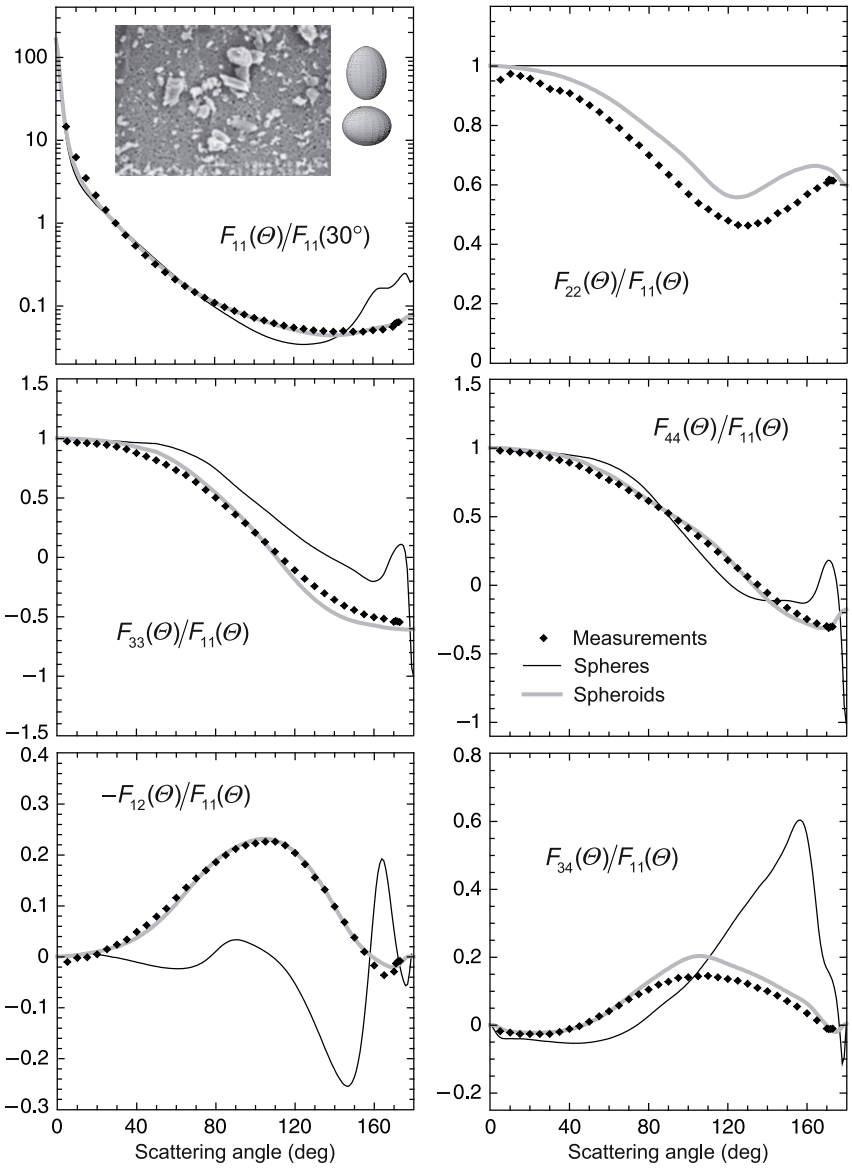

Figure 2.18 The diamonds depict the results of laboratory measurements of the ensemble-averaged Stokes scattering matrix for micrometer-sized feldspar particles at a wavelength of 633 nm (Volten et al., 2001). The grey curves show the result of fitting the laboratory data with *T*-matrix results computed for a shape mixture of polydisperse, randomly oriented prolate and oblate spheroids. The real and model particle shapes are contrasted in the inset. The black curves show the corresponding results for volume-equivalent polydisperse spherical particles.

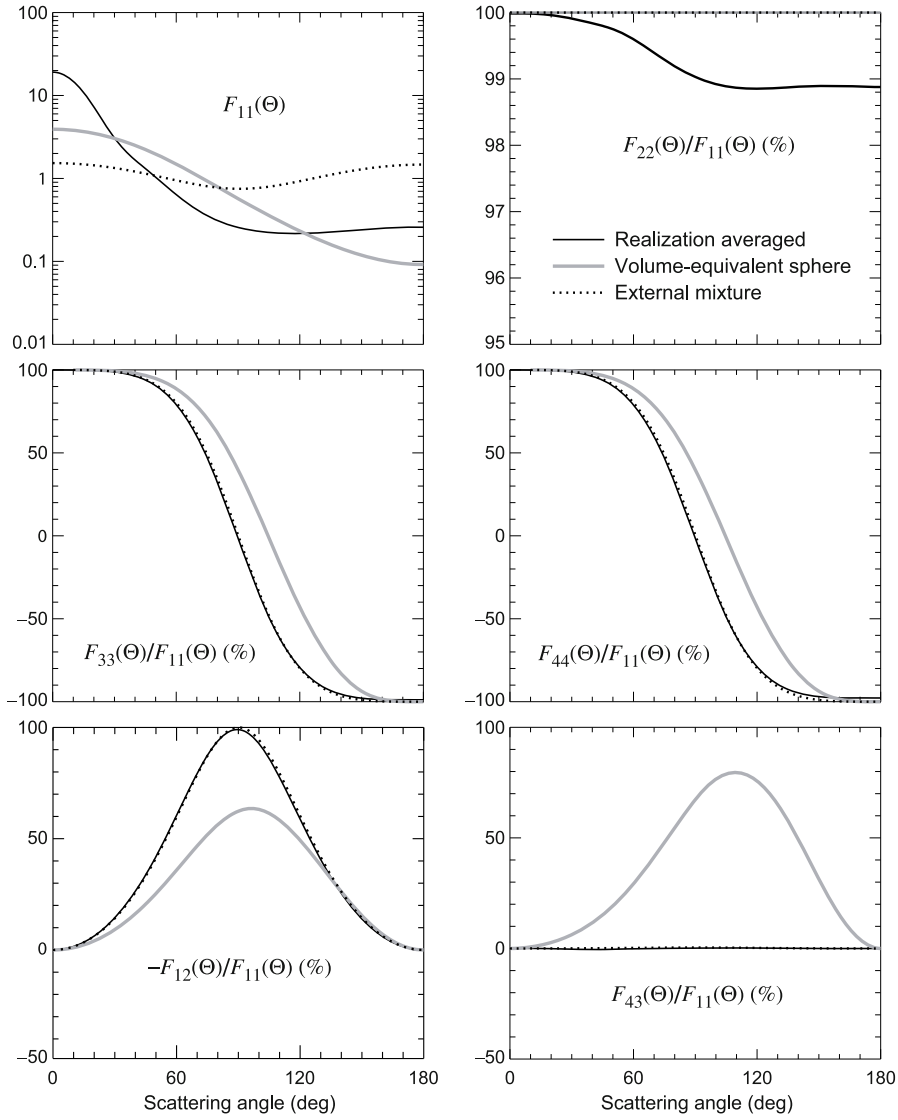

Figure 2.19 Realization-averaged scattering matrix elements for randomly oriented fractal clusters with $D_f = 1.82, k_0 = 1.19, N_s = 400$, and a = 0.02 μm. The soot refractive index is 1.75 + i0.435 and the wavelength of the incident light is 628 nm. Also shown are Lorenz–Mie results for the corresponding homogeneous volume-equivalent sphere and the "equivalent" external mixture of soot monomers.

Also depicted in Figure. 2.19 are two sets of approximate computations. The first one is the result of applying the single-scattering approximation to the corresponding external mixture of the constituent monomers (i.e., by assuming that all monomers are widely separated and randomly positioned rather than form a cluster with touching components). The second set was computed by applying the Lorenz–Mie theory to a homogeneous sphere with a volume equal to the cumulative volume of the cluster monomers. Clearly, the external-mixture model provides a poor representation of the cluster phase function, whereas the performance of the equal-volume-sphere model is inadequate with respect to all scattering matrix elements.